Back-Projecting Secondary Craters Using a Cone of Uncertainty

Timothy J. Naegeli[a,*], Jason Laura[b]

[a] *Penn State MGIS Program, 2305 Connelly Cir, Burnsville, MN 55337*
[b] *U.S. Geological Survey, Astrogeology Science Center, 2255 N. Gemini Dr., Flagstaff, AZ 86001*

Abstract

In this paper we present an extension to the Large Crater Clustering (LCC) tool set which places a cone of uncertainty around the trajectories of secondary impact craters to determine potential locations of source craters. The LCC tool set was a first step in the spatial quantification of primary and secondary cratering processes, which allows planetary geologists to accurately estimate the geologic age of a celestial surface. This work builds on the LCC tool set by accounting for the ambiguity of flight path trajectories through a Python script that leverages ArcGIS's ArcPy library. We chronicle the mechanics of the script, which creates geodetically correct cones then counts them within equally sized cells of a vector grid. We describe the process that was used to derive the shape of the cone and provide parameters for the sizes of the cones and the grid. We demonstrate that the cone of uncertainty has the ability to compensate for error in secondary crater trajectories by introducing deviation in the trajectory bearing and comparing the predicted primary crater location. We use two study areas on Mars as well as the entire

*Corresponding Author
Email address: `tbn5056@psu.edu` (Timothy J. Naegeli)

lunar surface to illustrate the usefulness of the extension as an aid to human interpretation of back-projections.

Keywords: GIS, Uncertainty, Planetary Science, Python, Astrogeology, Impact Craters

PACS: 96.12.Bc, 96.12.Kz, 96.20.Br, 96.20.Ka, 96.30.Gc

2000 MSC: 52A10, 53C22, 62M30, 65C05, 65C10, 68N15, 85-04, 86A32

1. Introduction

Crater counting, crater size frequency distribution assessment, and the identification of the relationship between primary and secondary craters are tools used to determine the age of a celestial body (Shoemaker et al., 1963; Barlow, 1988; McEwen and Bierhaus, 2006; Robbins and Hynek, 2014, 2012; Platz et al., 2013). Shoemaker (1962) identified secondary craters, those resulting from ejecta being propelled from a primary impact to be deposited elsewhere on the surface, as one of the main issues of using crater size-frequency distributions for temporal analysis. These secondaries contaminate crater counts to bias the data in a given area toward older geologic dating. The distinction of primary versus secondary craters must be approximated in order to perform accurate surface aging, and allows an opportunity to further our understanding of cratering processes.

Primary and secondary craters have distinctive patterns, morphologies, sizes, and orientations that provide opportunities for traditional spatial analysis (McEwen and Bierhaus, 2006; Laura et al., 2017). The average impact angle of a primary impact crater is approximately 45° (Shoemaker, 1962; McEwen and Bierhaus, 2006) and results in secondary impact craters with a range of impact angles and morphologies (McEwen and Bierhaus, 2006). McEwen and Bierhaus (2006) suggest that secondary impacts are frequently smaller ($<5\%$ of primary impact diameter), shallower, and more elliptical than primary craters, appearing to have been scooped out from the surface. Spatially, secondary craters can often be found in a tight ring around the primary that formed them or clustered in rays emanating from the primary (Preblich et al., 2007; McEwen et al., 2003). The shape of secondary clusters, catenae, and lineaments provide a means to estimate the primary crater location by back-projecting a trajectory either through multiple features (polylines) or through semi-major axes of bounding ellipses (clustered point data or crater clusters digitized as bounding ellipses) and locating intersections between these trajectory estimations. Back-projecting secondary craters can be done through a combination of human interpretation (McEwen et al., 2003) and geospatial analysis (Laura et al., 2017).

Skinner and Nava (2011) and Laura et al. (2017) identify the need for a quantitative method to study primary and secondary cratering. The Large Crater Clustering (LCC) tool set was developed to respond to this need. The LCC tool set transforms user supplied, secondary craters into trajectories which are back-projected along great circle arcs to estimate potential source crater locations. The tool set represents a first step in quantitatively examining secondary to primary crater flight trajectory relationships and provides a means to further studies that seek to empirically quantify and constrain secondary ejecta flight properties. The LCC tool set is comprised of the following five tools (processing steps) to support primary location estimation: (1) calculating the nearest-neighbor distances among a set of independently digitized input crater features, (2) using these distances to identify clusters of craters, (3) fitting an ellipse to bound the clusters, (4) back-projecting the ellipse along the semi-major axis to produce a flight path trajectory, and (5) intersecting these trajectories (polylines) to estimate the primary impact (Laura et al., 2017). When features are digitized as polyline or bounding ellipses the tool can begin running at step four. In conjunction with the LCC tool, Laura et al. (2017) implement a value-by-alpha visualization developed by Roth et al. (2010a) that uniformly buffers secondary trajectories to some user defined distance and utilizes the transparency (or alpha) component of the buffered geometry to support visual identification of areas of highest intensity, and therefore most likely primary impact location.

The LCC tool set has spatial analysis issues that can result in significant ambiguity in quantitative primary impact crater identification. Laura et al. (2017) identify issues regarding digitization, the impact of cluster outliers, edge effects, and the Modifiable Areal Unit Problem (MAUP)[1] (O'Sullivan and Unwin, 2010). In this work we directly address the error in the resulting trajectories and comment on the MAUP in the search for primaries. This paper describes our extension to the LCC tool set which places a cone of uncertainty around the projected secondary flight trajectory to account for ambiguity in ejecta flight paths and in the digitization process.

The balance of this paper is arranged as follows. In Section 2 we describe a Python script that fits a cone of uncertainty to secondary crater trajectories. In Section 3 we describe a simulation which introduces sources of trajectory

[1]Bias in the analysis resulting from the placement of the study area boundary or the scale that was used.

error in a test area to evaluate the effectiveness of the cone. Section 4 explores three case studies, one from the Moon and two from Mars, to evaluate the cone of uncertainty in real scenarios. Finally, in Section 5, we comment on the validity of the cone of uncertainty and look ahead to future work.

2. Methods

In this work, we address issues of ambiguity in back-projection through the use of the cone of uncertainty and provide quantitative methods for the computation and interpretation of trajectory intersections. Using the back-projected secondary flight trajectories (from the LCC tool) we create two outputs: (1) a cone of uncertainty fit around each trajectory and (2) a vector grid whose values represent the number of overlapping cones. The former seeks to account for spatial ambiguity and digitization bias and the latter seeks to reduce the need for visual identification of high trajectory intersection locations, i.e., qualitative interpretation. In this section, we describe the selection of shapes the uncertainty buffer may take and the implementation of the LCC extension.

The cone of uncertainty is perhaps most widely known in tropical storm forecasting, where an event's location becomes increasingly uncertain with time and distance. In this construct the cone serves as an aid to forecast the future. Figure 1 shows the basic construction of a cone of uncertainty. When looking at secondary craters we view the same phenomenon in reverse. In this case the event has already occurred with a known endpoint but an unknown starting point. The best fit flight path of ejecta has increasing uncertainty as the distance from the secondary (toward the starting point) increases. By looking at an individual crater feature, we can create a cone with increasing width away from the feature representing the greater uncertainty of its origin. The uncertainty in secondary crater flight trajectories is known to exist with constraints developed by Popova et al. (2007), but there is currently no quantitative method that exists to incorporate this uncertainty into the back-projection process.

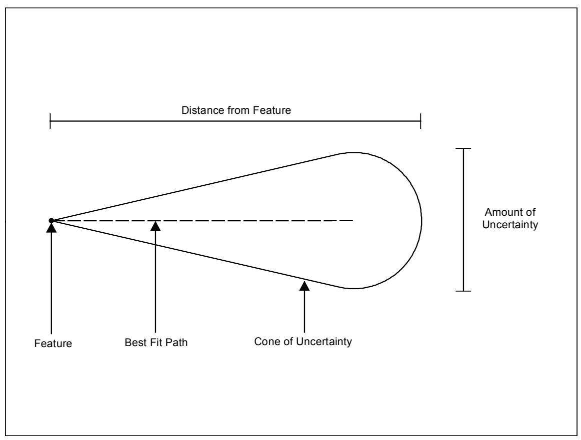

Figure 1: Cone of uncertainty shown as a shape that follows a best-fit trajectory. Width of the cone corresponds to the amount of uncertainty in the best-fit path, where a wider shape represents greater uncertainty.

2.1. Cone of Uncertainty Creation

We have extended the LCC tools by creating a Python (van Rossum and Drake, 2016) script which uses the output of the fourth processing step, a set of vector features representing the back-projection, to fit a cone of uncertainty around the trajectory and ultimately estimate the primary impact. The creation of the cone has four basic steps: (1) creating the trajectory within the LCC tool set, (2) buffering the endpoints of the trajectory, (3) creating a convex hull to encapsulate the space, and (4) adjusting the shape of the hull to account for the curvature of the surface. These four steps are depicted in Figure 2.

Use of the LCC tool and the creation of the line trajectory is described by Laura et al. (2017). The output of the LCC back-projection tool is a bi-directional line, with each segment ending at the secondary crater. In most cases, and without additional geomorphic knowledge of the feature, it is unknown from which direction along the semi-major axis the ejecta flew (McEwen and Bierhaus, 2006). The second phase of the cone creation, shown in (b) of Figure 2, buffers the starting and ending points of the trajectory. These buffers establish limits on the size of the cone where larger buffers indicate larger cones and greater uncertainty. More specifically, the amount of uncertainty is given by the size of the buffer around the starting point of the trajectory, the furthest point from the secondary. The buffer is a geodetic circle with a user defined radius. The user has the ability to enter multiple buffer sizes. If multiple sizes are entered, a separate layer of cones will be created for each entered size. The buffer for the end of the trajectory, near the secondary, is a small standard circle that represents the minimal amount of uncertainty in the region. The small buffer also prevents potential overlap with the ending buffer of the other half of the bidirectional line for that secondary.

The next step creates a polygonal shape to encapsulate the line endpoint buffers. The two buffers are merged into one multipart polygon, then a convex hull[2] envelops the space around it by wrapping around the outside

[2]The smallest shape that can be created that contains all given points where no line

half of each buffer and connecting in between them. The convex hull allows the amount of uncertainty to uniformly increase from the secondary to the buffer around the starting trajectory. This is depicted in (c) of Figure 2. The resulting shape is a planar hull that follows the projection being used but not the shape of the surface, therefore the distance to the trajectory is unequal along the entire feature and in some cases the trajectory may be outside the hull. The final step in the cone creation process corrects for this by altering the hull so that it represents the shortest distance along the surface and follows the path of the trajectory. The final output is shown as (d) in Figure 2.

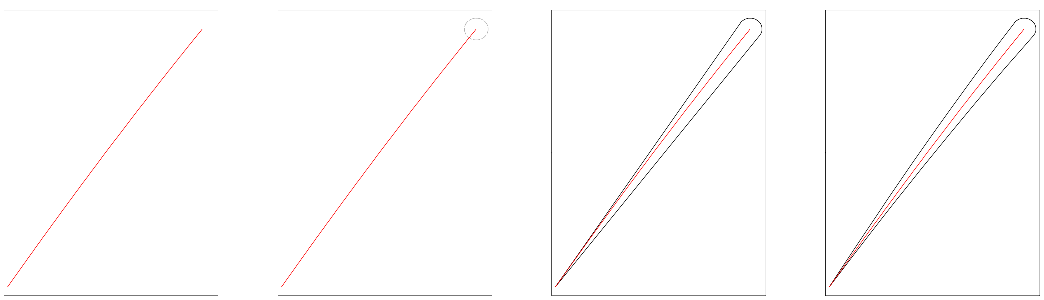

(a) Trajectory (b) Buffer (c) Convex Hull (d) Final Cone

Figure 2: Four basic steps in building the cone of uncertainty are (a) the starting trajectory (b) buffering the starting point according to a user-defined distance (c) creating a convex hull of the shape (d) geodetically altering the hull to arrive at the final cone.

2.2. Counting Intersecting Cones

Once the cones have been created, the final section of the LCC extension script focuses on identifying source craters by counting the number of

drawn between those points extends outside the shape.

cones that intersect with a uniform grid. This is a similar concept to the Value-By-Alpha approach developed by Roth et al. (2010b) and described for use in identifying primary craters by (Laura et al., 2017). While Laura et al. (2017) sifted for primaries qualitatively, the grid approach taken in the LCC extension aims to suggest source craters quantitatively. Our extension supports exploration of issues of scale (MAUP) by allowing for multiple runs with differing cell sizes to create a more complete picture of the crater relationships. The grid approach aids in human interpretation by allowing the user to identify patterns within the study area. Examples of interpretation of the data using this method are given in Section 4.

Counting the overlapping cones is a three step process using the LCC extension: (1) creating a grid, (2) performing a spatial join between the layer of cones and the grid, and (3) depicting the resulting number of counts. These three steps are illustrated in Figure 3. The extension requires an initial specification of a projection for subsequent processing. The data from the LCC tool set should be re-projected to an equal-area projection to ensure the grid cells are of equal size. Other projections may distort the grid sizes and resulting cone counts.

The analysis grid is created by utilizing the fishnet function within the ESRI ArcGIS ArcPy site package. The extent of the grid is set to match that of the original trajectory layer. A user defined size, input at the beginning of the script, determines the size of each grid cell. With the grid and cone layers in place, a spatial join is performed that counts the number of features in the cone layer that overlap with each feature (cell) in the grid. A new layer is created, having identical spatial properties as the grid, which

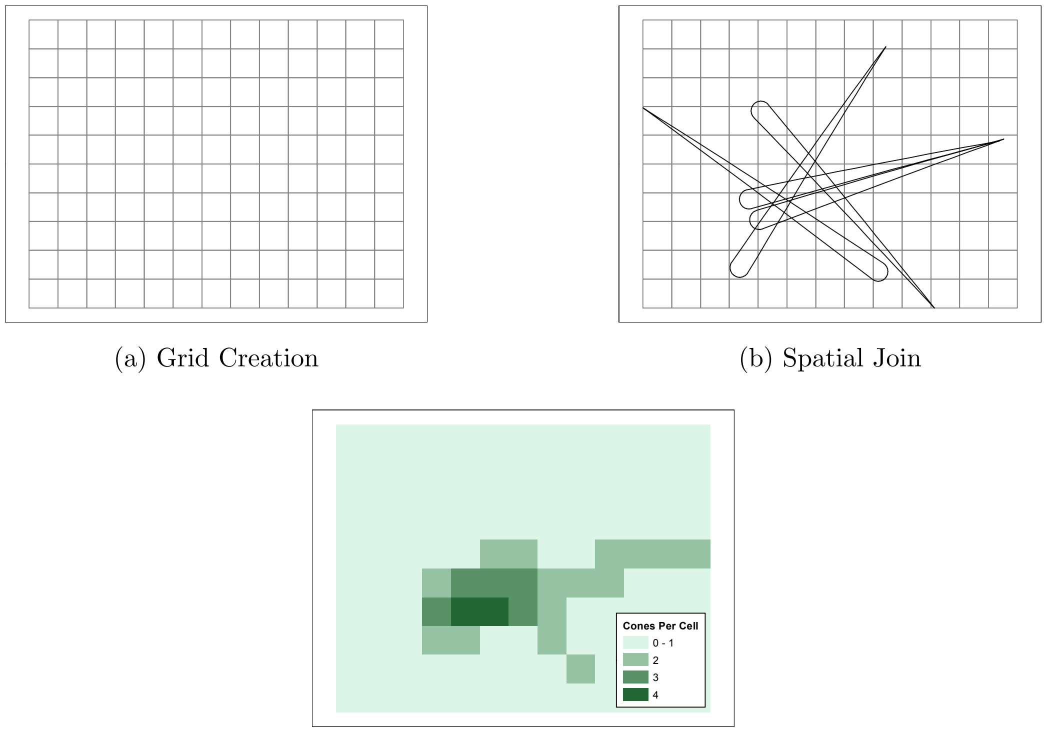

(a) Grid Creation

(b) Spatial Join

(c) Intersections

Figure 3: Quantitatively searching for a primary crater is a three step process: (a) creating a grid (b) intersecting it with the trajectory cones (c) thematically representing the overlap counts.

contains this count. In order to make use of this information, the data are exported out to an ArcMap .mxd document. The method of classification and thematic representation occur external to the LCC extension. Examples of these depictions are shown in Sections 2.3, 3, and 4.

2.3. Testing and Parameterization

We empirically tested five cone of uncertainty shapes with the goal of determining which would be the best predictor of a primary crater. These shapes were designed to test which area(s) along the trajectory typically intersect the source crater and how the size of the shape affected predictability. The first round of testing was intended to compare the cone against the theoretically most predictive sections of the line trajectory. Figure 4 illustrates each of the five tested shapes with the initial polyline depicted at the center. These shapes are as follows:

1. A single uniform buffer, intended to show some variability in the line trajectory that does not deviate with distance. This is the simplest fit around a trajectory and was selected as a 'proof of concept' of using a shape, in lieu of a line, to predict a primary. When compared to the output of the cone test this geometry provides an idea of how strong the middle of the cone predicts a primary relative to its periphery.
2. A circular buffer placed around the starting point (point opposite the secondary), or beginning of the modeled flight path, where the primary crater should be. This buffer is similar to the widest section of the cone and allows us to see how accurate this portion of the shape is, and how well the length of the LCC line can pinpoint the primary. We note that that the LCC trajectory tool supports user defined trajectory length, making estimation using this method a function of both the selected buffer size and the user defined flight distance length.
3. A uniform cone, the classic shape from hurricane modeling, where the girth becomes wider as the distance away from the secondary increases. This was the most intuitive shape because of the uncertainty of the trajectory between the secondary and primary. In theory this shape should be the most predictive so if shapes (1) or (2) are significantly

more predictive the cone will need to be altered.

4. A cone given a weight corresponding to the ellipticity of the secondary crater feature. The less predictive, circular crater clusters receive a cone that has a lower weight. It was an attempt to see if the cone could be improved by tying the overlap count to the ellipticity of the cones rather than the number of cones. If successful, it should significantly improve the prediction of Zunil.
5. A nested cone which keeps the intuitive cone approach but gives higher weight to the middle and end of the trajectory, the area near the trajectory and closest to the secondary, which are the most predictive aspects of the cone as determined from the first three shapes. In practice this is not one cone but three on top of each other so a grid cell intersecting the last half of the trajectory line would be given a count of three, not one as in the case of the uniform cone. Thus it implicitly gives more weight to those parts of the cone deemed most predictive.

Each shape was fit around trajectories created in the LCC tool set from a sample of known secondaries originating from Zunil Crater, Mars. Figure 4 displays these basic shapes, their fit to the Zunil trajectories, and the overlap counts for each of the tests. As explained in Section 2.2, the highest intersection counts per cell suggest the location of a primary, in this case Zunil, and are displayed with darker shading. The red circle is the actual location of Zunil.

Of the three initial shapes, only the starting point circular buffer was unable to suggest the general location of Zunil. It is assumed then that the uncertainty near the beginning of the trajectory is relatively large. How-

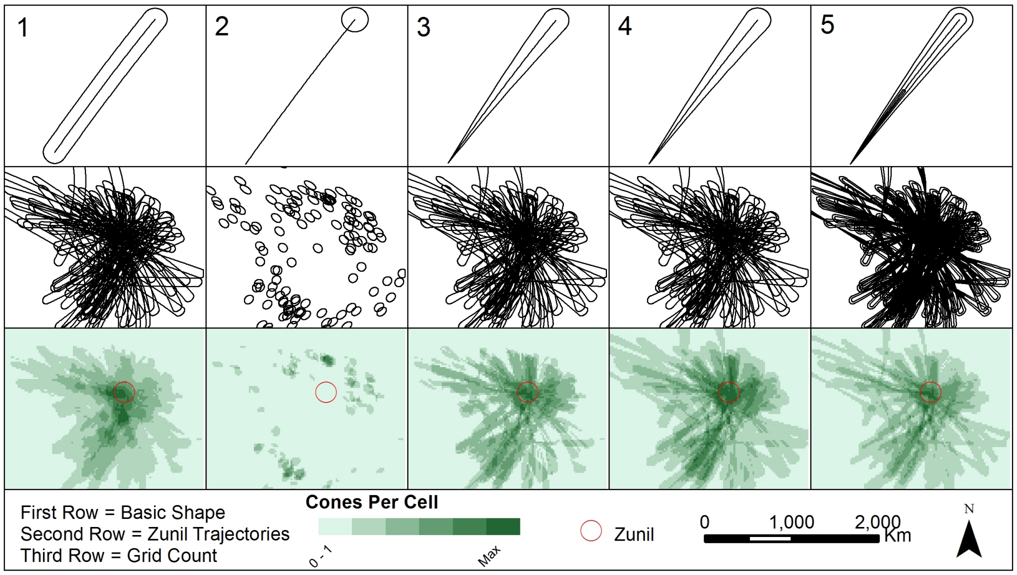

Figure 4: Basic cone shape, shape placed around Zunil secondary trajectories, and overlapping shape counts for (1) simple uniform buffer, (2) circular buffer around beginning of trajectory, (3) uniform cone, (4) weighted cone based on ellipticity, and (5) nested cone. Uniform cone is the best compromise of source crater predictability and script run time.

ever, it should be noted that other crater systems may align well with the beginning of the modeled flight path. Looking at the location of Zunil and the other shapes it is clear that Zunil is typically within the last half of the trajectory. The uniform buffer and cone both predicted the general location of Zunil. The cone was more precise in its prediction, and has a more intuitive shape given the distance-uncertainty relationship described in Section 2. Therefore we determine from these three initial tests that the cone can be used to predict the location of a source crater, and that the area closest to the trajectory and away from the starting point are the most predictive. With this knowledge, we tested two additional methods to see if the cone could be improved.

The cone shape based on ellipticity was not significantly more predictive of Zunil than the uniform cone, and required additional run time. Within the LCC tool the user has the ability to place a threshold on the ellipticity of secondary features when creating the trajectories, and therefore we suggest including a cutoff here to include only those trajectories whose directional distribution can be confidently assumed. While it is the most complete picture of the trajectory, the successes of the nested cones are offset by the increased required storage and run time. Therefore, the uniform cone was selected as the final shape, having the most desirable trade-off between predictability, run time, and disk space.

The usefulness of the LCC extension is tied not only to the shape of uncertainty being used, but the size that shape takes as well as the grid that counts it. For the cone it is assumed that the uncertainty near the secondary crater is low and thus the minimum width is essentially zero, as the location of the secondary is known without modeled ambiguity. Popova et al. (2007) suggest that the maximum width dispersion of a given set of secondaries from a primary (e.g., a single trajectory) is at most 25 kilometers. We utilize this constraint as a starting point in cone selection. While a known trajectory may have a width dispersion of 25 kilometers, we must expand this value to account for ambiguity in the digitization and trajectory estimation processes. For the Zunil system, cones having starting trajectory buffer diameters of 5, 10, 25, 50, and 100 kilometers were tested. The resulting cones counted over a grid with 400 square kilometer cells is shown in Figure 5. With no significant difference in run time, larger cones tended to distill the overlaps down to a useful level.

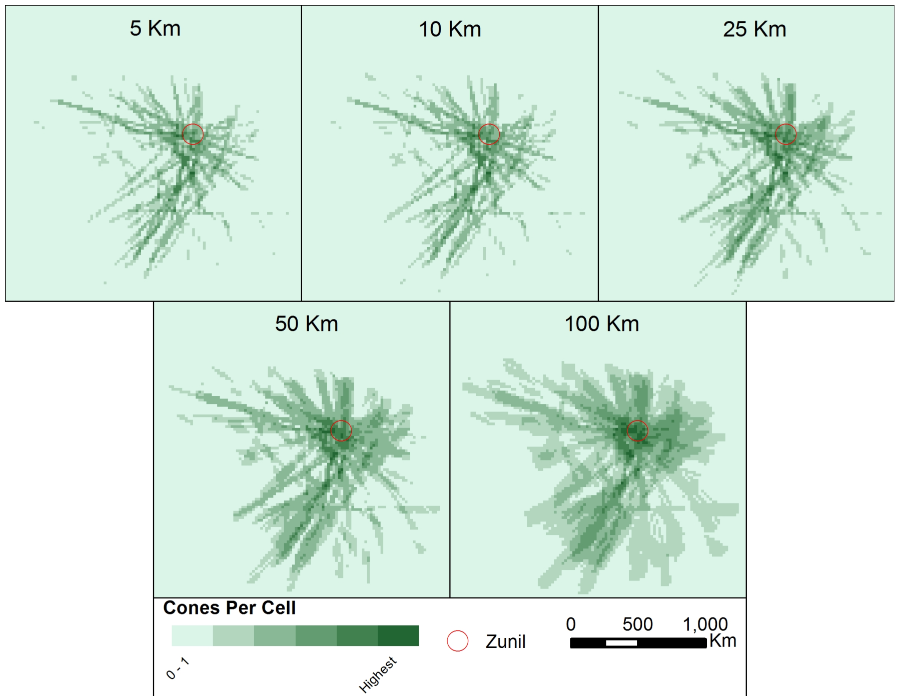

Figure 5: Cones of various sizes enumerated against a grid with 400 square kilometer cells in the Zunil test area. The largest cones create the most intersections and a more complete picture of the region.

The grid cell size is dependent on the spread of trajectories, the amount of detail required by the user, and the amount of run time desired. To test the size of the grid cells counting the cone intersections, cones having a maximum width of 50 kilometers were intersected with grids having cell sizes of 25, 100, 400, 2,500, and 10,000 square kilometers for the Zunil test area. The results of this test are shown in Figure 6. The two smallest grid cell sizes created numerous areas without intersections and made visual pattern recognition more difficult. The two largest grid cell sizes tended to mask much of the useful detail for human interpretation. The grid with 400 square kilometer cells provided the best compromise of detail and run time.

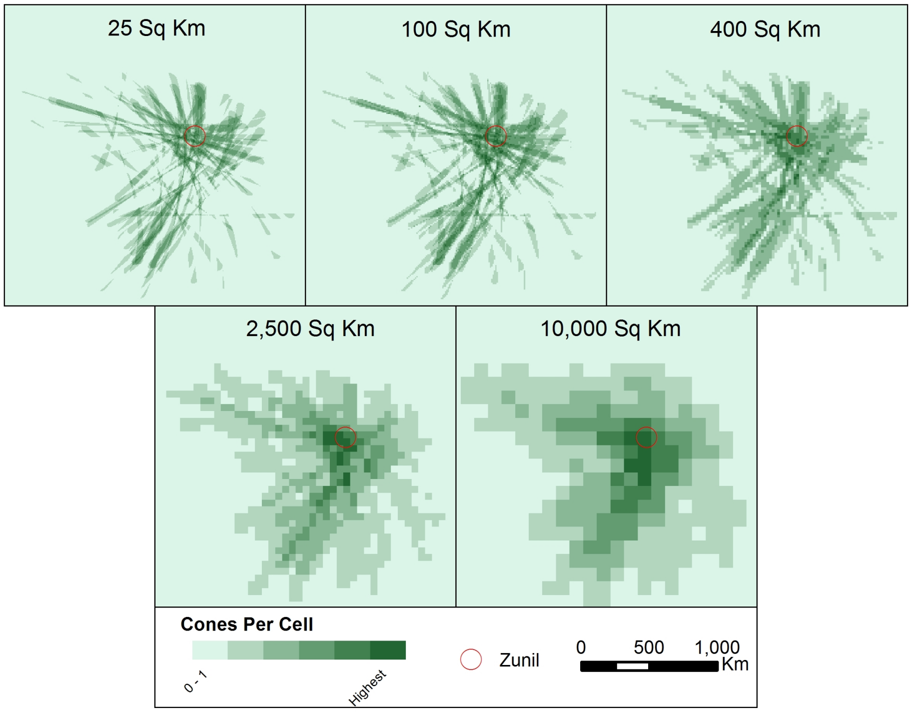

Figure 6: 50 kilometer cone of uncertainty enumerated against grids of varying cell sizes in the Zunil test area. Largest grid sizes run fastest, but with least detail.

Table 1 shows the increasing amount of time required for more granular cells. It also shows the runtime for cones of various sizes run over a 400 square kilometer grid. The algorithm is more sensitive to the resolution of the grid cell and the number of grids being run. The balance of run time and detail required will depend on the user and system. The user has the ability to run multiple cone and grid options simultaneously, and may choose to do so to establish the most useful combination. It is recommended that the user try several cone sizes and compare the output to gather the most information possible for the area at hand. A suggested default for a grid size in a Martian quadrangle is 400 square kilometer cells.

Cone Size (Km)	Grid Size (Sq Km)	Runtime
50	10,000	x
50	400	1.3x
50	25	7.0x
50	25, 100, 400, 2,500, 10,000	9.3x
5, 10	400	1.1x
5, 10, 25	400	1.1x
5, 10, 25, 50	400	1.2x
5, 10, 25, 50, 100	400	3.4x

Table 1: Script runtime for Zunil secondaries with various cone and grid selections.

3. Accounting for Uncertainty

3.1. Sources of Error

The usability of the cone of uncertainty in back-projecting secondary craters is contingent on its effectiveness in identifying the location of source craters and compensating for error in the trajectory itself. A line back-projection is a best estimate of a dynamic process having uncertainty arising from the following factors:

- Inevitable uniqueness in the individual secondary crater trajectories
- Continually developing science in the flight path of impact ejecta

- Uncertainty in the digitization of crater features

Although the first source of error almost certainly will exist, it is difficult to capture the deterministic randomness that any flight path might have. There has been significant research to understand impact and ejection events, and the resulting craters. Please see Vickery (1986, 1987), Popova et al. (2007), Melosh (1984), and Schultz and Gault (1985) for the details of this research. The error associated with the digitization is a combination of the skill, knowledge, and attention to detail of the user and the spatial resolution of the imagery from which the digitization is developed.

3.2. Error Simulation

We have run a series of Monte Carlo simulations that attempt to mimic the error identified in Section 3.1. The Zunil secondary crater trajectories were replicated 500 times, with each replication adjusting each trajectory between -10° and +10° sampled from a uniform random distribution. The trajectories themselves are shown in Figure 7 along with the simulated trajectories. Cones having 50 kilometer diameters were fit to each trajectory within these simulations and the overlaps were counted within a grid having 400 square kilometer cells. For each simulation, the grid cell containing the highest number of overlaps was identified then combined with the maximum cell from every other iteration. This was repeated with cones having a diameter of 100 kilometers. If the cone is successful in compensating for the introduced error, the maximum cell should be consistent throughout the iterations and drift should be minimal.

The two images in Figure 8 show the cells that had the maximum number of overlaps in at least one iteration, with the count representing the number

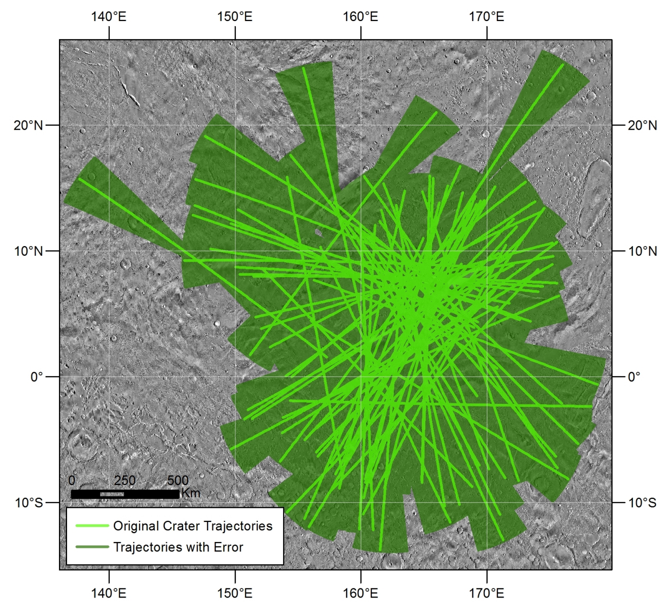

Figure 7: Original trajectories from Zunil with trajectories of 500 error-induced simulations.

of simulations where that cell was the max. Many iterations had multiple cells with the maximum count, so the totals are greater than 500. The red circle is the actual location of Zunil. In general the amount of drift in the maximum cells is minimal and the vast majority of iterations predict Zunil well. In both the 50 kilometer and 100 kilometer cone cases, the area of maximum overlap tends to be within a block of cells west of Zunil.

There is a cell near 160° east, 0° north that often contains the maximum number of overlaps, although with increased cone size it becomes less of a driver. When the cone has a starting diameter of 50 kilometers, there are several areas of cells containing the maximum overlaps with most near Zunil. When the cone is increased to 100 kilometers in diameter, the maximum cells consolidate considerably and most of the outlying cells are eliminated.

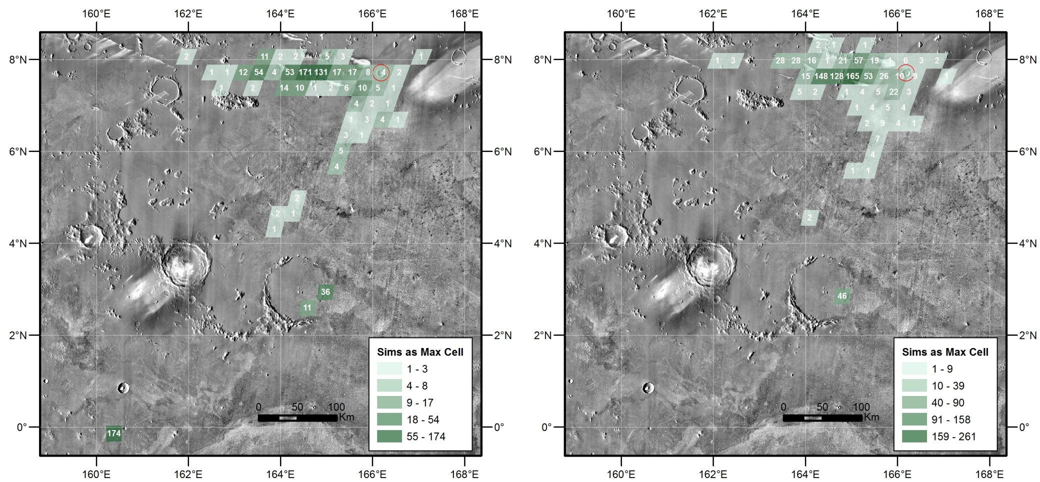

(a) 50 Km Cone

(b) 100 Km Cone

Figure 8: Cells having the maximum count of overlapping cones in at least one of 500 simulations that induce error. Count on each cell represents the number of simulations where it was the maximum.

Without prior knowledge of Zunil, it is reasonable to assume that a user could identify it as the source crater for the secondaries in the test dataset. In Figure 9 the max cell per test iteration using 100 kilometer cones is shown with the crater database created by Robbins and Hynek (2012) which contains the location of nearly 400,000 craters having a diameter of one kilometer or greater. Only three craters from the Robbins and Hynek (2012) dataset are within a maximum cell, with Zunil being one of them. However, Zunil falls within a cell that is the maximum in only ten simulations. It is more likely that for a given iteration Zunil would not fall within the maximum cell but the trend of the grid cells intersection counts, as described in Section 2.3, would lead to an investigation of neighborhood craters. With research such as McEwen et al. (2003) and Preblich et al. (2007), identification of Zunil is possible.

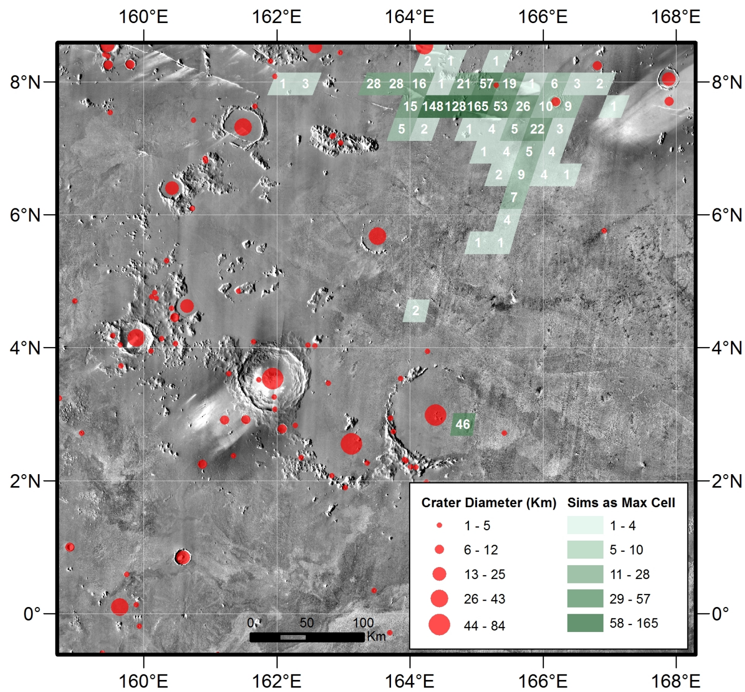

Figure 9: Maximum cells from the 100 kilometer cone error simulation shown with craters having a diameter over one kilometer.

3.3. Implications

This simulation represents a first phase, best case scenario. Nearly all of the trajectories are based on craters known to be Zunil secondaries, so there is a strong bias of the trajectories to merge toward Zunil. McEwen et al. (2003) showed that Zunil secondaries occur in tight clusters within rays and thus it is likely that the amount of error here is lower than in other systems. This should not invalidate the ability of the cone to compensate for error. Cone size needs to reflect a number of assumptions which will be suited to the crater system being studied. Here we show that the cone of uncertainty can lead to a consistent result. It should not provide pass to ignore accuracy requirements but provide insurance that the end result is correct.

4. Case Studies

As stated previously, the ability of using shapes to effectively identify source craters is a key measurement in assessing the effectiveness of this representation. In addition to the Zunil testing discussed in Sections 2 and 3, three case studies were used to examine whether the cone of uncertainty can locate known source craters. In each case the LCC tool was used to create polyline back-projections, then a cone having a diameter of 50 kilometers at the trajectory starting point was created and the subsequent overlaps were enumerated over a grid of 400 square kilometer cells. Each case study below is accompanied by a map of these overlaps, with the darker shading indicating a higher number of intersections.

Two of these case studies come from areas on Mars, Mare Acidalium and Lunae Palus, which were used by Laura et al. (2017). This provides a means of comparing the visual interpretation with and without the cone of uncertainty. The digitization of craters used for these regions was based on CTX (Malin et al., 2007) and THEMIS (Christensen et al., 2004) imagery having a spatial resolution of eight meters and 100 meters per pixel, respectively. In this paper we describe an additional case study, the entire surface of the moon, as an example from a separate surface and scale. The craters in the lunar dataset was digitized using the Wide Area Camera (WAC) (Robinson et al., 2011) mosaic and a Lunar Orbiter Laser Altimeter (LOLA) (Smith et al., 2010) derived Digital Terrain Model (DTM).

4.1. Acidalia

The Mare Acidalium quadrangle lies in the northeastern plains of the Martian western hemisphere, bounded by 30° to 60° north latitude and 0° to 60° west longitude. There were a total of 44 bi-directional trajectories (88 trajectories total) examined in Mare Acidalium based on secondary crater clusters whose bounding ellipse had an inverse flattening less than two. No minimum threshold was placed on the length of the trajectory, in order to keep a robust data set. The resulting cone overlap counts are shown in Figure 10. This data set provides the first opportunity to use the cones of uncertainty in a setting with multiple primary craters.

There are two areas in Mare Acidalium that strongly suggest the existence of a primary crater. The first, denoted as A1, is located in the vicinity of 29° west, 43° north and the second, denoted as A2, is located in the vicinity of 46° west, 40° north. These areas represent clusters of overlapping cones which intersect at different angles. There are areas which have higher counts as a result of parallel cones in close proximity. The areas northeast and southwest of A1 are such examples that are likely areas of contamination, identified from the pattern in the grid, rather than a string of primaries. There is likely only one or two primaries in the line from 40° west, 30° north to 20° west, 50° north and one is A1. From that line of concentration there is another line connecting it to A2. That intersection is another potential primary. There is likely some contamination, but here the counts are not continuous throughout. There are two concentrated pockets, at roughly 42° west, 38° north and 40° west, 36° north that potentially hold a primary. A final area of interest exists near 14° west, 39° north where the count is not particularly high but is unique compared to the surrounding area and appears it is the result of trajectories from at least two directions.

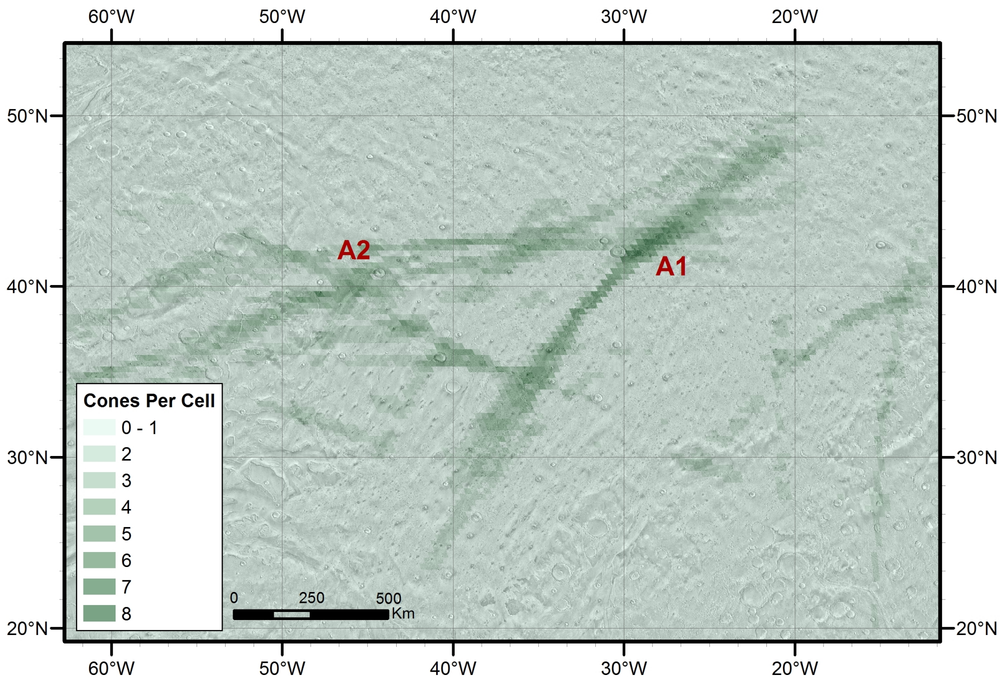

Figure 10: Grid counting overlapping cones of uncertainty in the Mare Acidalium quadrangle, Mars.

4.2. Lunae Palus

The Lunae Palus quadrangle lies in the east-central region of the Martian western hemisphere, bounded by 0° to 30° north latitude and 45° to 90° west longitude. Clusters, catenae, and lineaments were back-projected using the LCC tool for a total of 537 bi-directional trajectories (1,074 single directional trajectories). No restrictions were placed on the features and all craters were back-projected. The resulting cone overlap counts are shown in Figure 11.

There are several areas in Lunae Palus that suggest the presence of a primary crater. The first is located near 87° west, 22° north with the highest number of overlaps in the entire region. The second strongest candidate is near 51° west, 3° north. It seems likely that there are other primaries in close proximity. These potentials are near 53° west 11° north, 49° west 8° north, and 57° west 5° north. These could be areas of cone contamination or viable primaries. A final area worth investigating exists near 68° west, 18° north. These are the strongest candidates. There are likely many other primaries that exist in Lunae Palus given the number of grid intersections. This data set is unique relative to the other study sites in that the number of trajectories is much higher, so there could be areas with a unique localized count suggesting a primary that is not readily obvious upon visual inspection at a small scale.

4.3. Moon

There were a total of 4,981 secondary crater clusters, catenae, and lineaments from the entire lunar surface that were back-projected using the LCC tool without the Coriolis Effect, then the cones were created and intersected. The resulting map is shown in Figure 12. There are many areas that clearly suggest primary craters, most notably at 20° west, 10° north and at 0° west, 36° north. Most interestingly, and unique to this data set, is that there are areas of negative space where very few intersections exist. The most prominent example of this is centered at roughly 92° west, 22° south. Looking at the pattern of intersections around this feature, and directed away from it, suggests that this is an impact basin much larger than any grid cell.

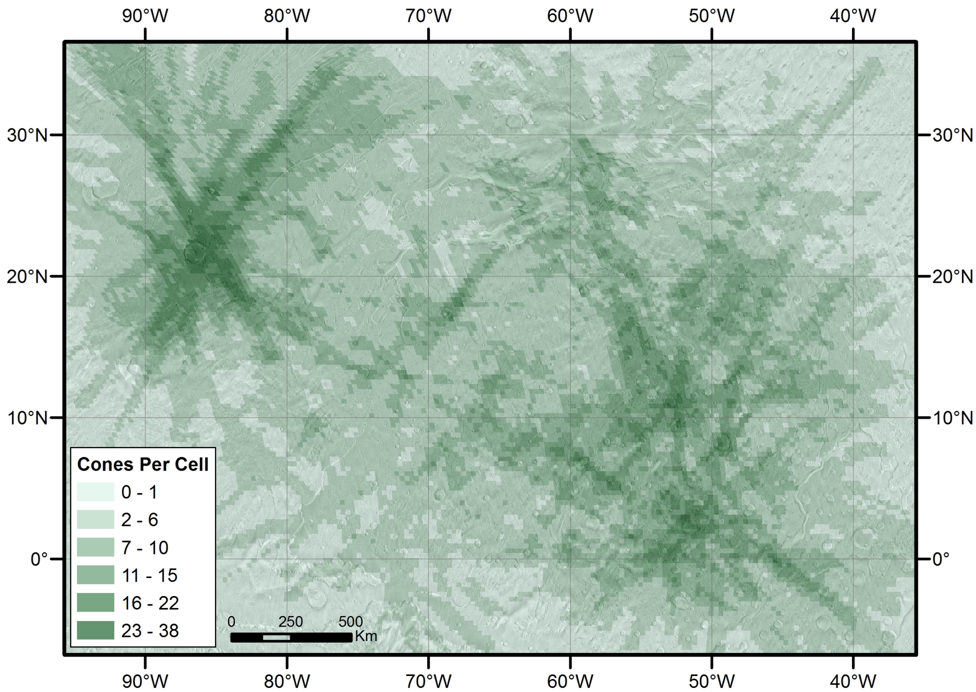

Figure 11: Counts of overlapping cones of uncertainty in the Lunae Palus quadrangle, Mars.

4.4. Commentary on Case Studies

With the exception of the lunar data, the case studies presented here are common in that they place borders in borderless worlds. The Zunil test case in particular is biased in that the data are known to be related to Zunil and few craters independent of Zunil are presented. It may be the case that a study area with a wider scope makes it more difficult for primaries to be identified. However, we have seen in the lunar data that in a worldwide data set primaries are still identifiable. We caution, then, against the selection of a very refined study area.

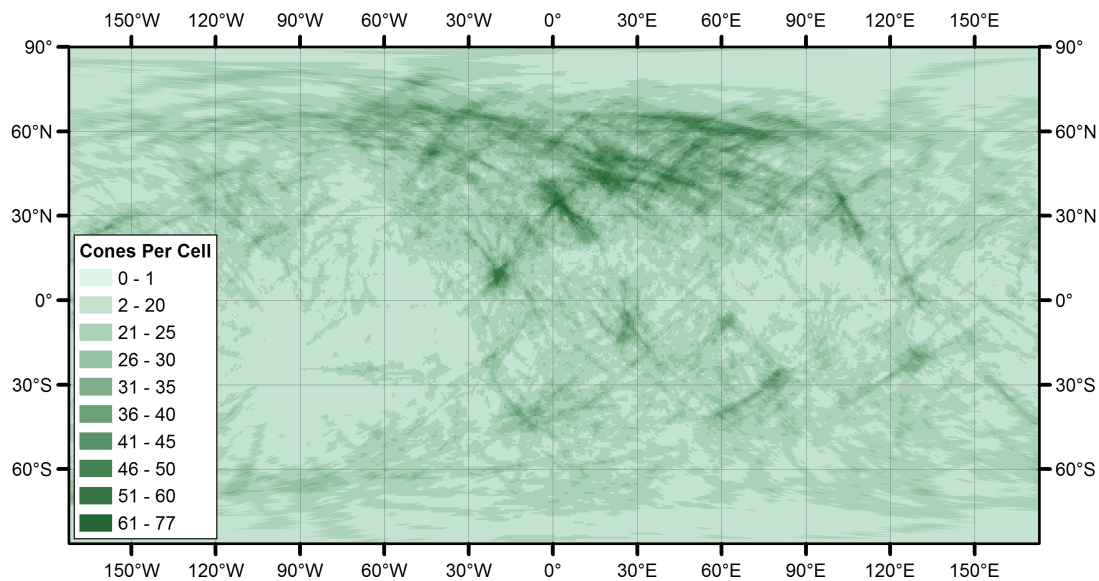

Figure 12: Counts of overlapping cones of uncertainty across the entire lunar surface.

5. Conclusions

In this paper we have established the cone of uncertainty as a meaningful tool in back-projecting secondary craters to identify source craters. The LCC tool extension is openly available as a Python script designed to seamlessly use the output from the LCC tool set. Along with the description of the construction of the cone the code is open to contribution and refinement. We have tested this LCC tool extension on three areas of Mars as well as the moon, and have demonstrated its ability to compensate for trajectory error, address the MUAP, and quantitatively assess source impact locations.

We anticipate the application of using cones during back-projection will be immediately useful to anyone searching for source craters. It takes us one step closer in merging the worlds of impact science and crater studies for geological analysis. These sciences are, naturally, continually developing and should unite to provide a more holistic view of past and current planetary bombardment. Despite this more automated, quantified view there still exists a strong need for human interpretation throughout the process. This paper serves as another tool to support that function.

As the LCC tool was a first step in the quantification of back-projecting, so too is the implementation of the cone of uncertainty a first step in accounting for trajectory error. We identify four opportunities for future work in this area. First, the quantification of the amount of potential error in the trajectories would be useful quality assurance and in identifying the selection of the cone parameters. Second, more testing around the uncertainty should be undertaken. Each crater system will provide unique challenges and differing amounts of error. Testing multiple systems, and on multiple bodies, will help further refine the cone parameters. Third, the cone parameters should be refined scientifically. This paper analyzed the problem of back-projecting from primarily a spatial point of view, and scientific guidelines should be provided to increase its usability. Finally, whether using polyline or cone back projections, each secondary is being associated with one or more primaries. Given the Monte Carlo simulation undertaken herein and the ability to use those simulations to quantify the probability of a secondary to primary association, we intend to explore iteratively removing secondaries from the analysis pool as they are associated with a primary.

6. Acknowledgement

Any use of trade, firm, or product names is for descriptive purposes only and does not imply endorsement by the U.S. government.

References

Barlow, N., 1988. Crater size-frequency distributions and a revised martian relative chronology. Icarus 75 (2), 285–305.

Christensen, P. R., Jakosky, B. M., Kieffer, H. H., Malin, M. C., Jr, H. Y. M., Nealson, K., Mehall, G. L., Silverman, S. H., Ferry, S., Caplinger, M., Ravine, M., 2004. 2001 Mars Odyssey. Springer Netherlands, Dordrecht, Ch. The Thermal Emission Imaging System (Themis) for the Mars 2001 Odyssey Mission, pp. 85–130.
URL http://dx.doi.org/10.1007/978-0-306-48600-5_3

Laura, J., Skinner, J. A., Hunter, M. A., 2017. Large Crater Clustering Tool. Computers & Geosciences 105, 81–90.
URL https://doi.org/10.1016/j.cageo.2017.04.011

Malin, M. C., Bell, J. F., Cantor, B. A., Caplinger, M. A., Calvin, W. M., Clancy, R. T., Edgett, K. S., Edwards, L., Haberle, R. M., James, P. B., Lee, S. W., Ravine, M. A., Thomas, P. C., Wolff, M. J., 2007. Context camera investigation on board the mars reconnaissance orbiter. Journal of Geophysical Research: Planets 112 (E5), n/a–n/a, e05S04.
URL http://dx.doi.org/10.1029/2006JE002808

McEwen, A., Turtle, E., Burr, D., Milazzo, M., Lanagan, P., Christensen, P., Boyce, J., Team, T. T. S., 2003. Discovery of a large rayed crater on mars: Implications for recent volcanic and fluvial activity and the origin of martian meteorites. Lunar and Planetary Science XXXIV, abstract 2040.

McEwen, A. S., Bierhaus, E. B., 2006. The Importance of Secondary Cratering to Age Constraints on Planetary Surfaces. Annual Review of Earth and Planetary Science 34, 535–567.

Melosh, H., 1984. Impact Ejection, Spallation, and the Original of Meteorites. Icarus 59, 234–260.

O'Sullivan, D., Unwin, D. J., 2010. Geographic Information Analysis. Wiley, Hoboken, New Jersey.

Platz, T., Michael, G., Tanaka, K. L., Jr., J. A. S., Fortezzo, C. M., 2013. Crater-based dating of geological units on Mars: Methods and application for the new global geological map. Icarus 225 (1), 806 – 827. URL `http://www.sciencedirect.com/science/article/pii/S0019103513001863`

Popova, O. P., Hartmann, W. K., Nemtchinov, I. V., Richardson, D. C., Berman, D. C., 2007. Crater clusters on Mars: Shedding light on martian ejecta launch conditions. Icarus 190 (1), 50–73.

Preblich, B. S., McEwen, A. S., Studer, D. M., 2007. Mapping rays and secondary craters from the Martian crater Zunil. Journal of Geophysical Research 112 (E05006).

Robbins, S. J., Hynek, B. M., 2012. A new global database of Mars impact craters 1 km: 1. Database creation, properties, and parameters. Journal of Geophysical Research 117 (E05004).

Robbins, S. J., Hynek, B. M., 2014. The secondary crater population of mars. Earth and Planetary Science Letters 400 (Supplement C), 66 – 76. URL `http://www.sciencedirect.com/science/article/pii/S0012821X14002994`

Robinson, M. S., Denevi, B., Sato, H., Hapke, B., Hawke, B., 2011. LROC WAC ultraviolet reflectance of the Moon. Lunar Planet.Sci. XLII, Abstract 1842.

Roth, R. E., Woodruff, A. W., Johnson, Z. F., 2010a. Value-by-alpha maps: An alternative technique to the cartogram. The Cartographic Journal 47 (2), 130–140.
URL http://dx.doi.org/10.1179/000870409X12488753453372

Roth, R. E., Woodruff, A. W., Johnson, Z. F., 2010b. Value-by-alpha Maps: An Alternative Technique to the Cartogram. The Cartographic Journal 47 (2), 130–140.

Schultz, P. H., Gault, D. E., 1985. Clustered Impacts: Experiments and Implications. Journal of Geophysical Research 90 (B5), 3701–3732.

Shoemaker, E. M., 1962. Interpretation of Lunar Craters. In: Physics and Astronomy of the Moon. Academic Press, New York, pp. 283 – 359.

Shoemaker, E. M., Hackman, R. J., Eggleton, R. E., 1963. Interplanetary Correlation of Geologic Time. Advances in Astronautical Sciences 8, 70–89.

Skinner, J. A., Nava, R. A., 2011. Using Large Crater Clusters to Identify Potential Source Craters on Mars: Technical Methods and Science Applications, Abstract #2502. In: Lunar and Planetary Science Conference. Vol. 42 of Lunar and Planetary Science Conference.

Smith, D. E., Zuber, M. T., Jackson, G. B., Cavanaugh, J. F., Neumann, G. A., Riris, H., Sun, X., Zellar, R. S., Coltharp, C., Connelly, J., Katz,

R. B., Kleyner, I., Liiva, P., Matuszeski, A., Mazarico, E. M., McGarry, J. F., Novo-Gradac, A.-M., Ott, M. N., Peters, C., Ramos-Izquierdo, L. A., Ramsey, L., Rowlands, D. D., Schmidt, S., Scott, V. S., Shaw, G. B., Smith, J. C., Swinski, J.-P., Torrence, M. H., Unger, G., Yu, A. W., Zagwodzki, T. W., Jan 2010. The lunar orbiter laser altimeter investigation on the lunar reconnaissance orbiter mission. Space Science Reviews 150 (1), 209–241.
URL `https://doi.org/10.1007/s11214-009-9512-y`

van Rossum, G., Drake, F., 2016. Python Reference Manual. http://python.org.

Vickery, A., 1986. Size-Velocity Distribution of Large Ejecta Fragments. Icarus 67, 224–236.

Vickery, A. M., 1987. Variation In Ejecta Size With Ejection Velocity. Geophysical Research Letters 14 (7), 726–729.